Soft Matter

Accepted Manuscript

This is an *Accepted Manuscript*, which has been through the Royal Society of Chemistry peer review process and has been accepted for publication.

Accepted Manuscripts are published online shortly after acceptance, before technical editing, formatting and proof reading. Using this free service, authors can make their results available to the community, in citable form, before we publish the edited article. We will replace this *Accepted Manuscript* with the edited and formatted *Advance Article* as soon as it is available.

You can find more information about *Accepted Manuscripts* in the Information for Authors.

Please note that technical editing may introduce minor changes to the text and/or graphics, which may alter content. The journal's standard Terms & Conditions and the Ethical guidelines still apply. In no event shall the Royal Society of Chemistry be held responsible for any errors or omissions in this *Accepted Manuscript* or any consequences arising from the use of any information it contains.

ROYAL SOCIETY OF CHEMISTRY

www.rsc.org/softmatter

Colloidal transport and diffusion over a tilted periodic potential: dynamics of individual particles

Xiao-guang Ma[1], Pik-Yin Lai[2], Bruce J. Ackerson[3], and Penger Tong[1]
[1] Department of Physics, Hong Kong University of Science and Technology, Clear Water Bay, Kowloon, Hong Kong
[2] Department of Physics and Center for Complex Systems, National Central University, Chungli, Taiwan 320, ROC and
[3] Department of Physics, Oklahoma State University, Stillwater, Oklahoma 74078, USA
(Dated: November 15, 2014)

A tilted two-layer colloidal system is constructed for the study of force-assisted barrier-crossing dynamics over a periodic potential. The periodic potential is provided by the bottom layer colloidal spheres forming a fixed crystalline pattern on a glass substrate. The corrugated surface of the bottom colloidal crystal provides a gravitational potential field for the top layer diffusing particles. By tilting the sample at an angle θ with respect to the vertical (gravity) direction, a tangential component of the gravitational force F is applied to the diffusing particles. The measured mean drift velocity $v(F, E_b)$ and diffusion coefficient $D(F, E_b)$ of the particles as a function of F and energy barrier height E_b agree well with the exact results of the one-dimensional drift velocity [1] and diffusion coefficient [2, 3]. Based on these exact results, we show analytically and verify experimentally that there exists a scaling region, in which $v(F, E_b)$ and $D(F, E_b)$ both scale as $\nu'(F)\exp[-E_b^*(F)/k_BT]$, where the Arrhenius pre-factor $\nu'(F)$ and effective barrier height $E_b^*(F)$ are both modified by F. The experiment demonstrates the applications of this model system in evaluating different scaling forms of $\nu'(F)$ and $E_b^*(F)$ and their accuracy, in order to extract useful information about the external potential, such as the intrinsic barrier height E_b.

PACS numbers: 82.70.Dd, 05.10.Gg, 05.40.-a.

I. INTRODUCTION

Energy landscape is an important concept in science, which has been widely used in many areas of physics, chemistry and biology [4]. In surface science for instance, the motion of atoms adsorbed on a crystal surface (adatoms) under thermal agitations is determined by the electronic interactions with the substrate atoms [5–7]. In cell biology, the lateral motion of membrane-bounded proteins on a cell membrane is determined by a complex interaction landscape with the surrounding proteins and lipids and with the underlying cytoskeleton [8, 9]. In the study of protein folding, the change of protein configurations is thought of as a diffusion in a funnel-like energy landscape along the reaction coordinates [10, 11]. Our general understanding of this type of problem is through the well-known Arrhenius-Kramers equation [12, 13],

$$k = (k_0\nu)e^{-E_b/k_BT}, \tag{1}$$

which connects the reaction (or diffusion) rate k to the energy barrier height E_b with k_0 being an attempt frequency and ν the Arrhenius pre-factor. Equation (1) provides a simple physical picture for a common class of diffusive barrier-crossing problem. It is valid for reactions or transitions involving a large energy barrier, for example with $E_b/k_BT \gtrsim$ 6-7 [14–16].

The diffusive barrier crossing is made under constant thermal agitations and the probability for such random events to occur becomes very small if E_b is much larger than the thermal energy k_BT. This situation is changed completely when an external force F is applied to the particle, so that the energy barrier is lowered in the direction of forcing. Understanding the effect of the external force on thermally activated kinetics is a concern of a common class of transport problem, such as particle separation by electrophoresis [17, 18], electromigration of atoms on the surface of metals [19] and semiconductors [20], motion of a three-phase contact line under the influence of an unbalanced capillary force [21], control of crystal growth [22] and design of nano-scale machineries [23, 24]. In biology and biophysics, force-assisted thermal activation is employed in various single molecule stretching experiments to study the binding and folding energy landscape of bio-molecules, such as DNA [25], RNA [26], nucleic acids [27], receptors/ligands [28] and proteins [29], and the adhesion between bio-membranes of vesicles, capsules and living cells [30, 31].

To obtain useful information about the underlying energy landscape, such as the energy barrier height E_b, from the experiment, various theoretical models [30, 32–37] have been proposed; most of them are modified versions of the Arrhenius-Kramers equation. In developing these models and facilitating their applications in the experiment, a number of assumptions and approximations have been made at different levels in order to calculate how the Arrhenius factor ν and barrier height E_b change with the external force F. For many practical applications, however, one often encounters complications, such as highly hierarchical structures and heterogeneous kinetics [38], making it difficult to directly apply the sophisticated statistical mechanics models to connect the kinematics with the energetics [39–41]. While some models have been widely used to explain the experimental data, there are few experimental systems in which one can actually visualize the energy landscape and test the theory.

Thus much of the work done so far is through computer simulations. Finding an experimental model system in which one can directly measure the energy landscape and track individual particle trajectories with adequate statistics is, therefore, extremely valuable in testing different theoretical ideas.

Attempts have been made to use an external potential field to mimic the effect of an energy landscape, which is usually imposed by the surrounding molecules to a test particle. Examples include the study of colloidal transport and diffusion in a one-dimensional (1D) optical trap (optical tweezers) with either a periodic or random variation of the laser light intensity [42–45]. Recently, we developed a two-layer colloidal system to study colloidal diffusion over a periodic potential [16]. The periodic potential is provided by the bottom layer of colloidal spheres forming a crystalline pattern on a glass substrate. The corrugated surface of the colloidal crystal provides a gravitational potential field for the diffusing particles on the top layer. Using the techniques of optical microscopy and multi-particle tracking, we measured the population statistics of the diffusing particles and constructed the external potential via the Boltzmann distribution. The dynamical properties of the diffusing particle, such as its escape time and diffusion coefficient, were simultaneously measured from the particle's trajectories. With the simultaneously obtained energetics and dynamics information, we tested the theory and demonstrated the applications of the colloidal potential. This work opens up a new realm of investigation at the single-particle level for a range of interesting problems associated with the diffusive and force-assisted barrier-crossing dynamics over complex potentials.

In this paper, we report a systematic study of the effects of an external force F on the barrier crossing dynamics of the diffusing particles over a periodic potential. By tilting the entire two-layer system at an angle θ with respect to the vertical (gravity) direction, a tangential component of the gravitational force F is applied to the top layer particles. In the experiment, we measure the particle's mean drift velocity $v(F, E_b)$ and diffusion coefficient $D(F, E_b)$ as a function of F (by varying the tilt angle θ) and E_b (by using different colloidal samples). The experimental results are compared with the exact results of the 1D drift velocity [1] and diffusion coefficient [2, 3]. Based on these exact results, we show analytically and verify experimentally that there exists a scaling region, in which $v(F, E_b)$ and $D(F, E_b)$ both have an approximate Arrhenius-Kramers-like form, $\nu'(F)\exp[-E_b^*(F)/k_BT]$, where the Arrhenius pre-factor $\nu'(F)$ and the effective energy barrier height $E_b^*(F)$ are both modified by the external force F.

A primary objective of the paper is to find some approximate but simpler expressions for $v(F, E_b)$ and $D(F, E_b)$ in different scaling regimes, based on the exact results [1–3], and to delineate the proper conditions under which one can use these scaling results in the experiment to accurately extract the characteristics of the external potential, such as the intrinsic barrier height E_b. The remainder of the paper is organized as follows. We first describe the theory of the 1D Brownian dynamics of colloidal particles over a tilted periodic potential in Section II. The experimental procedures and image processing methods are presented in Section III. The experimental results and discussions are given in Section IV. Finally, the work is summarized in Section V.

II. THEORY

We consider the 1D motion of a Brownian particle of mass m under the influence of an external potential $U(x)$. The particle's motion can be described by the Langevin equation [46]

$$m\frac{d^2x}{dt^2} + \xi\frac{dx}{dt} = f_B(t) - \frac{dU(x)}{dx}, \tag{2}$$

where $x(t)$ is the particle's position at time t, $\xi dx/dt$ is the drag force experienced by the particle with ξ being the friction coefficient, and $f_B(t)$ is the random Brownian force due to thermal fluctuations of the surrounding fluid. While the mean value of $f_B(t)$ is zero, its autocorrelation function $C(\tau)$ is non-zero and has a form [47],

$$C(\tau) \equiv \langle f_B(t+\tau)f_B(t)\rangle = 2k_BT\xi\delta(\tau), \tag{3}$$

where k_BT is the thermal energy of the system and $\delta(t)$ is the δ-function. The last term, $-dU(x)/dx$, is the conservative force experienced by the particle resulting from the external potential. If the motion is over-damped, which is the case for colloidal particles in an aqueous solution, the first term in Eq. (2) can be omitted.

When there is an external constant force F acting on the particle and the potential $U_0(x)$ without forcing is periodic, one can find an exact solution of Eq. (2) [2, 3]. In this case, one has $U(x) = U_0(x) - Fx$, where $U_0(x) = U_0(x+\lambda)$ with λ being the period. The introduction of the external force F breaks the detailed balance and generates a net particle flux along the direction of F. After a short period of relaxation, the system reaches a steady state and the particles obtain a mean drift velocity v, which has the form [1]

$$v = \left[\frac{D_0}{\lambda}\right]\frac{1-e^{-F\lambda/k_BT}}{\frac{1}{\lambda}\int_0^\lambda dx I_+(x)}, \tag{4}$$

where

$$I_+(x) = \frac{1}{\lambda}\int_0^\lambda dy e^{[U(x)-U(x-y)]/k_BT}, \tag{5}$$

and $D_0 = k_BT/\xi$ is the particle's free diffusion coefficient without the influence of the potential $U(x)$. In the moving reference frame with the velocity v, the long-time

behavior of the particle's motion is diffusive and the diffusion coefficient D has the form [2, 3]:

$$D = D_0 \frac{\frac{1}{\lambda}\int_0^\lambda dx I_+^2(x) I_-(x)}{\left[\frac{1}{\lambda}\int_0^\lambda dx I_+(x)\right]^3}, \quad (6)$$

where

$$I_-(x) = \frac{1}{\lambda}\int_0^\lambda dy e^{[-U(x)-U(x+y)]/k_BT}. \quad (7)$$

While Eqs. (4) and (6) are the exact analytic results, their integration forms make it quite difficult to understand the physical meaning of these equations. In the following, we will use different approximations to simplify these equations, so that one can use them directly in the experiment.

A. Small force expansion

We first define a force unit associated with the thermal energy k_BT as $F_T \equiv k_BT/\lambda$. When $F < F_T$, both v and D can be expanded in terms of F/F_T and we find

$$v \simeq \frac{v_0}{R}\{1 + \frac{1}{2}\left(\frac{1}{3} - \frac{\int_0^\lambda dx K_+^{(0)}(x)}{\int_0^\lambda dx I_+^{(0)}(x)}\right)\left(\frac{F}{F_T}\right)^2 + \mathcal{O}\left[\left(\frac{F}{F_T}\right)^4\right]\}, \quad (8)$$

and

$$D \simeq \frac{D_0}{R}\{1 + 3\left(\frac{\int_0^\lambda dx I_+^{(0)}(x) J_+^{(0)}(x) J_-^{(0)}(x)}{\int_0^\lambda dx [I_+^{(0)}(x)]^2 I_-^{(0)}(x)} - \frac{1}{4}\right)\left(\frac{F}{F_T}\right)^2 + \mathcal{O}\left[\left(\frac{F}{F_T}\right)^4\right]\}, \quad (9)$$

where

$$R = \left[\frac{1}{\lambda}\int_0^\lambda dx e^{U_0(x)/k_BT}\right]\left[\frac{1}{\lambda}\int_0^\lambda dx e^{-U_0(x)/k_BT}\right], \quad (10)$$

$$I_\pm^{(0)}(x) = \frac{1}{\lambda}\int_0^\lambda dy e^{[\pm U_0(x) - U_0(x\mp y)]/k_BT}, \quad (11)$$

$$J_\pm^{(0)}(x) = \frac{1}{\lambda^2}\int_0^\lambda dy y e^{[\pm U_0(x) - U_0(x\mp y)]/k_BT}, \quad (12)$$

and

$$K_\pm^{(0)}(x) = \frac{1}{\lambda^3}\int_0^\lambda dy y^2 e^{[\pm U_0(x) - U_0(x\mp y)]/k_BT}. \quad (13)$$

In the above, $v_0 = F/\xi$ is the drift velocity of the particle over a flat incline ($U_0(x) = 0$). In the limit $F \to 0$, v vanishes and D recovers the form given by Lifson and Jackson [48]. Because of the symmetry, one has $v(-F) = -v(F)$ and $D(-F) = D(F)$.

Equation (10) can be further simplified if variations of $U_0(x)$ are much larger than k_BT for some values of x. Under the steepest descent approximation, one finds that both v and D have the Arrhenius-Kramers form [12, 13] at the lowest order of F/F_T,

$$v \simeq v_0 \nu e^{-E_b/k_BT}, \quad (14)$$

and

$$D \simeq D_0 \nu e^{-E_b/k_BT}. \quad (15)$$

In the above, E_b is the energy barrier height and $\nu = (|U_a'' U_b''|)^{1/2}\lambda^2/(2\pi k_BT)$ is the Arrhenius pre-factor, which contains the second derivatives of $U_0(x)$ at the energy minimum x_a and at the energy barrier x_b. From Eqs. (8) and (14), we find the effective friction coefficient via the equation $v = F/\xi_{eff}$, where ξ_{eff} has the form

$$\xi_{eff} = \xi R \simeq \frac{\xi}{\nu} e^{E_b/k_BT}. \quad (16)$$

In the above, ξ is the friction coefficient for a flat incline. When $F < F_T$, v is proportional to F (linear response) and thus ξ_{eff} is independent of F. With Eq. (16), the diffusion coefficient D in Eq. (15) can be written as the Stokes-Einstein form $D = k_BT/\xi_{eff}$.

For a given potential $U_0(x)$, there exists a critical force F_c, which is given by the positive root of $F_c = U_0'(x_c)$, where x_c is the inflection point of $U_0(x)$ given by $U_0''(x_c) = 0$. At the critical force F_c, the effective barrier to escape vanishes [32, 33]. When $F >> F_c$, one asymptotically recovers $v \simeq v_0$ and $D \simeq D_0$.

B. Steepest descent approximation for intermediate forces $F_T \lesssim F \lesssim F_c$

To simplify the expressions to be given below, we write $U_0(x) = (E_b/2)u(x)$ with the barrier height E_b being explicitly factored out and $u(x) \in [-1, 1]$ is a unit periodic function. Then the 2D integration in Eqs. (4) and (6) can be written as

$$\frac{1}{\lambda}\int_0^\lambda dx I_+(x) = \frac{1}{\lambda^2}\int_{R_1} d\mathbf{r_1} e^{-(E_b/2k_BT)g_1(x,y)}, \quad (17)$$

where $\int_{R_1} d\mathbf{r_1} \equiv \int_0^\lambda \int_0^\lambda dxdy$ and

$$g_1(x, y) \equiv u(x) - u(x + y) + \frac{2F\lambda}{E_b}y. \quad (18)$$

The 4D integration in Eq. (6) can be expressed as

$$\frac{1}{\lambda}\int_0^\lambda dx I_+^2(x) I_-(x) = \frac{1}{\lambda^4}\int_{R_2} d\mathbf{r_2} e^{-(E_b/2k_BT)g_2(x,y,w,z)}, \quad (19)$$

where $\int_{R_2} d\mathbf{r_2} \equiv \int_0^\lambda \int_0^\lambda \int_0^\lambda dxdydwdz$ and

$$g_2(x,y,w,z) = u(x) - u(x+y) - u(x+w) + u(x-z) + \frac{2F\lambda}{E_b}(y+w+z). \quad (20)$$

For high energy barriers ($E_b >> k_BT$), one can use the saddle point method to carry out the integrations in Eqs. (17) and (19) and obtain

$$\frac{1}{\lambda}\int_0^\lambda dx I_+(x) \simeq \frac{4\pi k_BT}{E_b}\frac{\exp[-\frac{E_b}{2k_BT}g_1(\mathbf{r_1^*})]}{[\det\,\partial^2 g_1(\mathbf{r_1^*})]^{1/2}}, \quad (21)$$

and

$$\frac{1}{\lambda}\int_0^\lambda dx I_+^2(x)I_-(x) \simeq \frac{(4\pi k_BT)^2}{E_b^2}\frac{\exp[-\frac{E_b}{2k_BT}g_2(\mathbf{r_2^*})]}{[\det\,\partial^2 g_2(\mathbf{r_2^*})]^{1/2}}, \quad (22)$$

where $\mathbf{r_1^*} \equiv (x_1^*, y_1^*)$ and $\mathbf{r_2^*} \equiv (x_2^*, y_2^*, w_2^*, z_2^*)$ are, respectively, the saddle points of $g_1(\mathbf{r_1})$ and $g_2(\mathbf{r_2})$. The location of the saddle points can be determined by

$$u'(x_1^*) = u'(x_1^* + y_1^*) = \frac{F\lambda}{k_BT}, \quad (23)$$

and

$$u'(x_2^*) = u'(x_2^*+y_2^*) = u'(x_2^*+w_2^*) = u'(x_2^*-z_2^*) = \frac{F\lambda}{k_BT}. \quad (24)$$

The determinants of the Hessian matrix $\partial^2 g(\mathbf{r}^*)$ at the two saddle points in Eqs. (21) and (22) are, respectively,

$$\det\left[\partial^2 g_1(x_1^*, y_1^*)\right] = -u''(x_1^*)u''(x_1^*+y_1^*), \quad (25)$$

and

$$\det\left[\partial^2 g_2(x_2^*, y_2^*, w_2^*, z_2^*)\right] = u''(x_2^*)u''(x_2^*+y_2^*)u''(x_2^*+w_2^*)u''(x_2^*-z_2^*). \quad (26)$$

To make further progress, one needs to know the functional form of $u(x)$. Hereafter, we use the trial function, $u(x) = \cos(2\pi x/\lambda)$, to evaluate the above equations. From Eq. (23) we find the location of the saddle point $\mathbf{r_1^*}$,

$$(x_1^*, y_1^*) = \left[\frac{1}{2} + \frac{1}{2\pi}\sin^{-1}\left(\frac{F}{F_c}\right), \frac{1}{2} - \frac{1}{\pi}\sin^{-1}\left(\frac{F}{F_c}\right)\right], \quad (27)$$

where the critical force $F_c = \pi E_b/\lambda$. Eq. (21) then becomes

$$\frac{1}{\lambda}\int_0^\lambda dx I_+(x) \simeq \frac{k_BT}{F_c\lambda}\frac{e^{E_b^*/k_BT}}{[1-(F/F_c)^2]^{1/2}}, \quad (28)$$

where

$$E_b^* = E_b\left[1-\left(\frac{F}{F_c}\right)^2\right]^{1/2} - F\lambda\left[\frac{1}{2} - \frac{1}{\pi}\sin^{-1}\left(\frac{F}{F_c}\right)\right] \quad (29)$$

is the actual barrier height of the new potential $U(x) = U_0(x) - Fx$. Under the influence of the external force F, the value of E_b^* is reduced compared with the original barrier height E_b of $U_0(x)$. Thus under the steepest descent approximation, Eq. (4) is simplified to the following scaling form,

$$v \simeq v_c\nu' e^{-E_b^*/k_BT}, \quad (30)$$

where $v_c = F_c/\xi$ and

$$\nu' = \left[1-\left(\frac{F}{F_c}\right)^2\right]^{1/2}. \quad (31)$$

The effective friction coefficient ξ_{eff} in this case becomes

$$\xi_{eff}(F) \simeq \xi\frac{F}{F_c\nu'}e^{E_b^*/k_BT}. \quad (32)$$

In the intermediate force range $F_T \lesssim F \lesssim F_c$, v is not a linear function of F anymore (linear response does not work here) and thus $\xi_{eff}(F)$ becomes a function of F.

Similarly, we find the location of the saddle point $\mathbf{r_2^*}$,

$$[x_2^*, y_2^*, w_2^*, z_2^*] = [\frac{1}{2} + \frac{1}{2\pi}\sin^{-1}\left(\frac{F}{F_c}\right), \frac{1}{2} - \frac{1}{\pi}\sin^{-1}\left(\frac{F}{F_c}\right), \frac{1}{2} - \frac{1}{\pi}\sin^{-1}\left(\frac{F}{F_c}\right), 0], \quad (33)$$

and the steepest descent approximation gives

$$\frac{1}{\lambda}\int_0^\lambda dx I_+^2(x)I_-(x) \simeq \frac{1}{2}\left[\frac{k_BT}{F_c\lambda}\frac{e^{E_b^*/k_BT}}{[1-(F/F_c)^2]^{1/2}}\right]^2, \quad (34)$$

Note that because the saddle point is located at the integration boundary $z^* = 0$ in the z direction, the steepest descent result is twice larger than it should be. Therefore, a factor of 1/2 is introduced in Eq. (34). Eq. (6) then becomes

$$D \simeq D_c\nu' e^{-E_b^*/k_BT}, \quad (35)$$

where $D_c = F_c\lambda/(2\xi)$. With Eq. (32), the diffusion coefficient D in Eq. (35) can be written as $D = F(\lambda/2)/\xi_{eff}$. While this is of the Stokes-Einstein form, the thermal energy k_BT is now replaced by the work $(F\lambda/2)$ done by the external force to the energy barrier.

For a periodic potential, the transition rate k over one period can be written as $k = k_+ - k_-$, where k_+ is the forward rate and k_- is the backward rate. Because $k_- = k_+e^{-F/F_T}$, one can assume that $k \simeq k_+$ when $F >> F_T$. In this case, Eq. (30) can be re-written as a rate equation

$$k \equiv v/\lambda = k_c\nu' e^{-E_b^*/k_BT}, \quad (36)$$

where $k_c = v_c/\lambda$. This rate equation has been derived previously [33–36], by assuming that the effect of the external force is to modify both the barrier height and prefactor in the Kramers' rate equation. Herein we provide

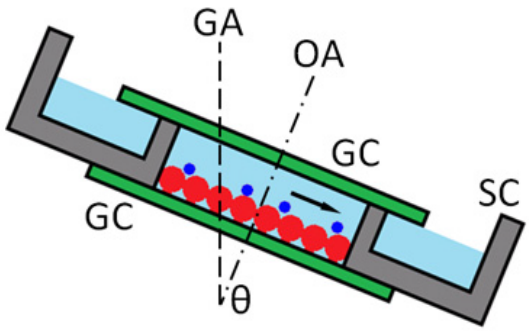

FIG. 1. (color online) Schematic diagram of the sample cell (side view): SC, stainless steel cell; GC, glass cover slip; GA, gravity axis; OA, optical axis; θ, tilt angle of the sample cell; red particles, large silica spheres forming a monolayer crystal on the bottom glass substrate; blue particles, smaller diffusing particles on top of the colloidal crystal; arrow, direction of force F acting on the diffusing particles.

a rigorous proof based on the exact solution as shown in Eqs. (4).

In addition, we also provide a direct proof of the scaling form of D based on the exact solution. Our results clearly demonstrate that the transport behavior of the particles driven by an external force F over a periodic potential $U_0(x)$ is governed by the actual barrier height E_b^* and the scaling factor ν'. In this case, the diffusion coefficient D scales with the particle-flux-induced diffusivity $D_c = F_c\lambda/(2\xi)$, which is independent of k_BT and can be much larger than the particle's free diffusion coefficient D_0. Furthermore, from Eqs. (4) and (6), and the steepest descent results in Eqs. (28) and (34), one obtains

$$\frac{v}{D} \simeq \frac{2}{\lambda}\left(1 - e^{-F/F_T}\right), \tag{37}$$

for $F/F_T > 1$. For $F/F_T < 1$, one finds $v \simeq (D/k_BT)F$.

In the experiment to be described below, we measure $v(F, E_b)$ and $D(F, E_b)$ as a function of F for different potentials $U_0(x)$. The experimental results will be compared with the approximate solutions discussed above. We will also examine the scaling behavior of the measured $v(F, E_b)$ and $D(F, E_b)$.

III. EXPERIMENT

A. Apparatus and sample preparation

Figure 1 shows the sample cell used in the experiment, which is tilted at an angle θ with respect to the vertical (gravity) direction. A central hole of 6 mm in diameter and 1 mm in depth is drilled through the center of a circular stainless steel cell (SC). The cell has a circular chamber of a slightly larger diameter surrounding the hole and is sealed from the bottom by a glass cover slip (GC). The entire sample cell has two fluid chambers; the central hole is used to hold the colloidal sample and the outer surrounding chamber contains additional solvent (water with the same salt concentration) to prevent sample evaporation. The central hole is first filled with the colloidal sample and is covered by another glass cover slip (GC). Under the action of capillary forces, the contact gap between the top cover slip and central sample cell (both are hydrophilic) is sealed by the sample solvent. The outer chamber is then filled with additional solvent, keeping the central sample chamber from being in contact with the outside air. In this way, sample evaporation is minimized so long as there is some solvent remained in the outer chamber. Extra solvent is added to the outer chamber from time to time during the experiment using an embedded syringe.

The sample cell is placed on the stage of an inverted microscope (Leica DM-IRB), and the motion of the particles is viewed from below using bright field microscopy. Movies of particle motion are recorded using a monochrome CCD camera (CoolSNAP, Media Cybernetics) and streamed to the hard drive of a host computer. They are taken at 7 frames per second. A commercial image acquisition software (ImagePro, Media Cybernetics) is used to control the camera. The recorded images have a spatial resolution of 1392×1040 pixels and 256 gray scales.

Plain silica spheres of different sizes are used in the experiment and they are purchased from Bangs Laboratories. All the purchased samples are thoroughly washed using deionized water by repeated centrifugation. The original aqueous solution of particles with 5% (g/mL) solid concentration is diluted at a 1:100 ratio by weight by deionized water. The solution is centrifuged at 1,000 rpm (at ∼100g centrifugal acceleration) for 5 minutes and the particles in the centrifuge sample settle down to the bottom of the test tube. The supernatant is then removed as much as possible using a pipet and the remaining solid is further diluted by deionized water for a repeated centrifugation. Typically, we repeat this procedure for 8-10 times to make sure that all the impurities in the solution are removed. To further remove the particle aggregates from the cleaned solution, we fill the solution in a thin test tube for free sedimentation until the interface between the supernatant and particle-containing solution falls to less than 1/2 of the original height. Then we pipet out a small amount of the solution just below the interface. The selected solution is found to contain only monodisperse silica spheres.

To prepare a close-packed monolayer of colloidal spheres near the bottom glass substrate, we add the colloidal solution into the sample cell one drop (∼200 μL) at a time until the area fraction n occupied by the silica spheres in the bottom layer reaches $n \simeq 0.7$. This process is monitored in real-time using a camera on the microscope and the particles take 1-2 minutes to settle on the glass substrate. The image analysis software Im-

TABLE I. Two colloidal samples used in the experiment with different pairs of top/bottom particles and the obtained external potential parameters, including lattice constant λ, energy barrier height E_b/k_BT, critical force F_c/F_T, and $R \equiv \langle \exp[U(x)/k_BT]\rangle_\lambda \langle \exp[-U(x)/k_BT]\rangle_\lambda$ (see text).

Samples	Top/bottom (μm)	$\lambda(\mu$m)	E_b/k_BT	F_c/F_T	R
S1	2.1/2.9	1.7	1.5	5.9±2	1.3
S2	3.6/3.6	2.1	6.7	22.8±2	40.0

agePro is used to calculate the area fraction n. Then a 1-mL syringe is used to continue the process with a smaller drop (10-20 μL) of the particle solution added at a time until n approaches the packing limit $n_c \simeq 0.8$. The sample is then left open for complete evaporation of water in the solution and the remaining particles are attached to the glass substrate by Van de Waals forces. The evaporation process takes several hours to complete at room temperature with a relative humidity of $\sim 70\%$.

During evaporation, the silica spheres self-assemble into a monolayer close-packed crystal patches. By laterally moving the sample stage, we are able to find a single crystal patch within the view area of $150\times113\mu m^2$, which is achieved by using a 63× oil objective. Then we fill the sample cell with a 0.1 mM aqueous solution of NaCl followed by addition of a drop of silica suspension into the salt solution using a 1 mL syringe. After several minutes, the silica spheres settle down on top of the bottom layer colloidal crystal, and the particle number in the view area is counted using ImagePro. This procedure is repeated until a desired area fraction n for the second layer particles is reached. The sample cell is then covered with a glass cover slip to prevent solvent evaporation. Two colloidal samples, S1 and S2, with different top/bottom particle sizes are used in the experiment and their properties are given in Table I.

B. Optical microscopy and image analysis

Figure 2 shows the silica spheres of diameter $d = 3.6\ \mu m$ (bright spots with a non-uniform intensity profile) diffusing over the bottom layer colloidal crystal (honeycomb lattice) made of the same silica spheres (sample S2). The image is taken with the focal plane located in between the two layers of silica spheres so that the out-of-focus image of the bottom colloidal crystal becomes a honey-comb lattice and the top diffusing particles appear as bright spots. The non-uniform intensity profile of the diffusing particles is caused by the interference with the bottom layer particles. The white arrow indicates the [1,0] crystalline direction of the bottom layer crystal.

The microscope is placed on a homemade incline with an adjustable tilt angle θ up to 35^0 with respect to the horizontal base. During the adjustment of tilt angle θ, the optical axis (OA) of the microscope, as shown in Fig. 1, is always kept perpendicular to the plane of the bottom colloidal crystal. Therefore, the focus plane of the objective does not change with increasing (or decreasing) θ. With this setup the external force F acting on the top layer diffusing particles is provided by gravity,

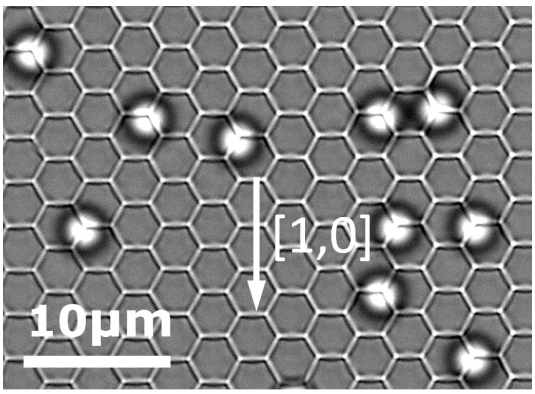

FIG. 2. Microscopic image of sample S2. The uniform honeycomb pattern in the background is the image pattern resulting from the bottom layer colloidal crystal. The bright spots with a non-uniform intensity profile are the diffusing particles on the top layer. The arrow indicates the [1,0] crystalline orientation. The scale bar is 10 μm.

$$F = \Delta m g \sin(\theta), \tag{38}$$

where Δm is the buoyant mass of the diffusing particles and g is the gravitational acceleration. For sample S2, we find $F \simeq (0.2pN)\sin(\theta)$. Note that because the potential $U_0(X)$ to be discussed below only involves the normal component of the gravity, $F_n = \Delta m g \cos(\theta)$, it does not change much for small values of θ. For example, at $\theta = 20^\circ$, we have $\cos(20^\circ) \simeq 0.94$.

For convenience, we rotate the CCD camera so that one pair of the rectangular boarders of the view area are exactly parallel to the direction of F. Thus we can use the boarders of the view area as the reference lines to align the crystalline orientation with respect to the direction of F by rotating the sample cell on the stage holder. For all the measurements to be discussed below, the direction of F is kept parallel to the [1,0] orientation of the bottom colloidal crystal.

By applying a standard Gaussian image filter from the Matlab image process toolbox, we can recover the uniform Gaussian-like intensity profile for each diffusing particle. The central position of the intensity profile is thus chosen as the center of the diffusing particle. With this method we are able to obtain a repeatable tracking accuracy of ∼1 pixel, which is 74 nm. A homemade Matlab program based on the standard tracking algorithm [49] is used to track the trajectory of the diffusing particles from consecutive images.

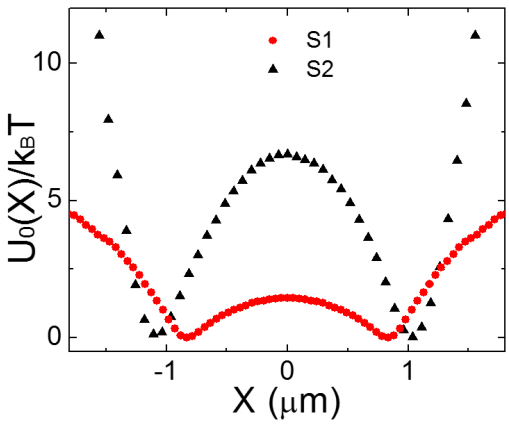

FIG. 3. (color online) Measured potential $U_0(X)/k_BT$ as a function of X for samples S1 (red solid circles) and S2 (black solid triangles).

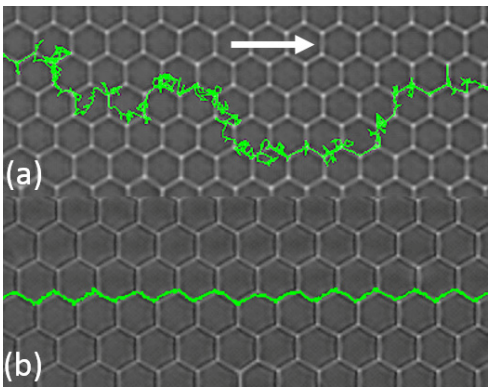

FIG. 4. (color online) Measured trajectory (green) of a diffusing particle over the bottom colloidal crystal for samples S1 (a) and S2 (b). The white arrow indicates the direction of the gravitational pulling force F.

IV. RESULTS AND DISCUSSIONS

A. Periodic potential

The method described in Ref. [16] is used to measure the periodic potential of the two colloidal samples. We find the occupation statistics of the top layer diffusing particles by adding together 10^5 images, each containing ∼100 particles, and counting the number of particles in each pixel. In doing so we obtain the population probability histogram (pph) $P(x, y)$ of finding a diffusing particle at location (x, y), which is related to the (gravitational) potential $U_0(x, y)$ over the rugged surface via the Boltzmann distribution,

$$P(x, y) \propto e^{-U_0(x,y)/k_BT}. \quad (39)$$

All the measurements are made at the area fraction $n \simeq 0.15$. At this area fraction, the interaction between the diffusing particles is negligibly small and Eq. (39) is valid [16]. Because the bottom layer is periodic, we divide the measured $P(x, y)$ into repetitive cells, each containing two nearby probability peaks together with a connecting valley. We then sum up the values of $P(x, y)$ from different cells with correct symmetry, and generate the single-cell pph $P_s(x, y)$, which has a higher statistical accuracy. Eq. (39) is then used to find the potential $U_0(x, y)/k_BT \simeq -\ln[P(x, y)]$. As will be shown below, the particle's trajectory follows a quasi-1D path X, and thus the 2D potential is simplified into a 1D potential $U_0(X)$.

Figure 3 shows the measured $U_0(X)$ for the two colloidal samples, S1 (red solid circles) and S2 (black solid triangles). The unit of X has been converted from pixels to micrometers using 1 pixel = 74 nm for our microscope setup. The measured $U_0(X)$ has a double-well structure with the distance λ between the two potential wells being given by $\lambda = d/\sqrt{3}$, where d is the diameter of the bottom layer spheres. The obtained value of λ from the measured $U_0(X)$ agrees well with that obtained from the honeycomb lattice pattern, as shown in Fig. 2. The energy barrier height E_b between the two potential wells and the critical force F_c are determined, respectively, by the maximum values of $U_0(X)$ and its first derivative $U_0'(X)$. The measured values of λ, E_b and F_c are given in Table I.

B. Steady-state probability distribution function of particle's displacement Δx

Figure 4 shows a comparison of particle's trajectories between sample S1 (a) with $F/F_T \simeq 1$ ($F_T \equiv k_BT/\lambda$) and sample S2 (b) with $F/F_T \simeq 4$. Also shown is the bottom colloidal crystal pattern, which serves as a visual guide of the underlying potential. The arrow indicates the direction of the gravitational pulling force F, which coincides with the [1,0] orientation of the bottom colloidal crystal as shown in Fig. 2. As will be shown below, when the forcing is along the [1,0] orientation, the particle's motion is essentially quasi-1D and thus we can compare the experimental results with the 1D theory as described in Sec. II. For other forcing directions, the particle's motion becomes increasingly 2D with increasing F. Hereafter, we focus our attention on the quasi-1D results, and we will report the 2D results elsewhere.

Figure 4(a) reveals several interesting features of the particle trajectories in sample S1. (i) At large length scales ($>> \lambda$), the particle drifts from the left to the right, following the direction of F. At smaller length scales ($< \lambda$), however, the particle spends most of its time diffusing within a potential well. The mean drift of the particles is thus caused by the break-down of the detailed balance between the forward barrier hopping and backward barrier hopping due to the external force. As a result, the mean velocity v of the particle becomes physically meaningful only when its traveling distance becomes larger than λ. (ii) Most of the barrier cross-

ing events take place between the two nearby potential wells. The particle has a higher probability to visit the transition paths which directly connect the two potential wells with a lower energy barrier, whereas occasionally it takes a path with a higher energy barrier. (iii) The particle also undergoes significant lateral barrier crossings; they are symmetric relative to F and their mean value over a long period of time tends to vanish. (iv) Backward hopping against the gravitational pulling force F is also observed but with a much lower frequency.

In contrast to sample S1 which only involves low energy barrier crossing with a small pulling force, sample S2 involves higher energy barrier crossing and a large pulling force and reveals some interesting new features as shown in Fig. 4(b). (i) The particle's trajectory follows a straight zig-zag path guided by the underlying low-energy path connecting the adjacent potential wells. (ii) The particle's trajectory is much more centered around the quasi-1D transition path connecting the two adjacent energy well without much spreading. (iii) Lateral barrier crossing is rarely observed in sample S2.

The difference in particle's trajectories between samples S1 and S2 can be explained as follows. For a leveled periodic potential (i.e., when $F = 0$), the particle has an equal probability to jump out of its current potential well and move into one of its three neighboring wells. However, when the sample is tilted with $F \neq 0$, the forward transition rate is increased by a factor of e^{F/F_T}, whereas the backward transition rate is reduced by a factor of e^{-F/F_T}. If one assumes that the 2D potential consists of many quasi-1D transition paths, the lateral transition rate will remain the same as that for the untilted sample with $F = 0$. Therefore, to observe a lateral hopping event, the particle's trajectory must have, on average, e^{F/F_T} forward moving jumps. In other words, the chance of observing lateral transitions becomes exponentially small with increasing F. For S2, the smallest tilting force is $F/F_T = 4$, and thus the chance of observing a lateral jump is only $e^{-4} \simeq 1.8\%$. For sample S1, however, the chance is significantly larger, as $e^{-1} \simeq 37\%$.

From the measured particle trajectories, we compute the probability density function (PDF) $G(\Delta x, \tau)$ of the particle's displacement, $\Delta x(\tau) = x(t+\tau) - x(t)$, over a lag time τ. To observe the particle's long-time dynamics, we deliberately take the value of τ to be larger than the mean-first-passage-time for the particle to crossover a single energy barrier. Figure 5(a) shows the measured PDFs as a function of $\Delta x(\tau)$ for sample S1 at $F/F_T = 2.4$ (titled angle $\theta = 9.2^o$) with three different delay times. The measured PDFs all have a shifted Gaussian shape with the most probable value of $\Delta x(\tau)$ increasing with τ. Figure 5(a) thus demonstrates that the diffusing particle over the tilted periodic potential undergoes a combined motion of random diffusion together with a mean drift velocity v. All the measured PDFs with different values

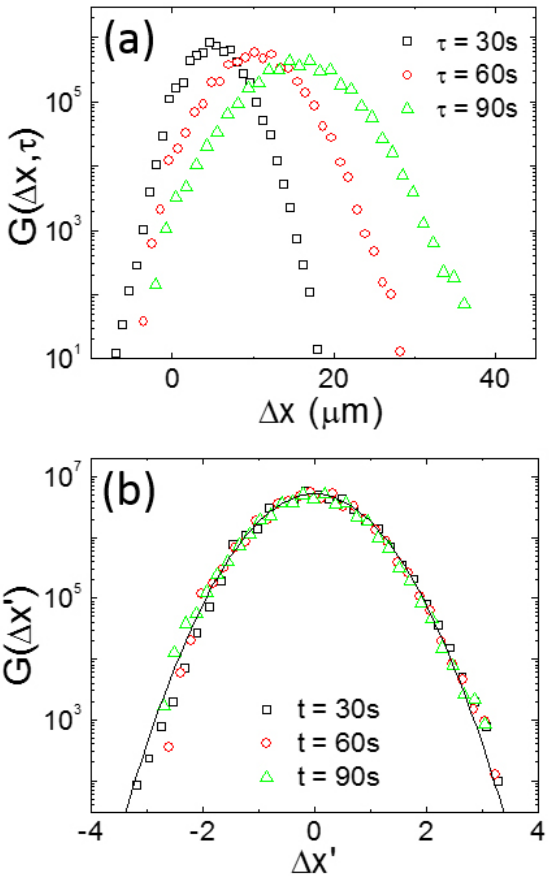

FIG. 5. (color online) (a) Measured probability density function (PDF) $G(\Delta x, \tau)$ of the particle's displacement $\Delta x(\tau)$ for sample S1 at $F/F_T = 2.4$ (titled angle $\theta = 9.2^o$) with three different delay times: $\tau = 30$ s (black squares), 60 s (red circles) and 90 s (green triangles). (b) Replot of the measured PDFs in (a) as a function of the normalized displacement, $\Delta x' = (\Delta x(\tau) - v\tau)/(2D\tau)^{1/2}$. The color code used is the same as that in (a). The solid line is a plot of Eq. (40).

of τ can be well described by the equation,

$$G(\Delta x, \tau) = G_0 e^{-\frac{1}{2}\left(\frac{\Delta x(\tau) - v\tau}{\sqrt{2D\tau}}\right)^2}, \qquad (40)$$

where G_0 is a normalization constant, and D is particle's diffusion coefficient. In the experiment, both v and D are used as the fitting parameters. Once the values of v and D are determined from the fitting, we find that all the measured PDFs can be collapsed into a master curve when they are plotted as a function of the normalized displacement, $\Delta x' = (\Delta x(\tau) - v\tau)/(2D\tau)^{1/2}$. Figure 5(b) shows the collapsed PDFs as a function of $\Delta x'$. The solid line is a plot of Eq. (40), which fits the data well.

In the above discussion, the direction of the pulling force F [see Fig. 4(a)] is denoted as the x-direction, and the direction normal to the x-direction is denoted as the y-direction. For sample S2, because the particle's tra-

jectories follow the zig-zag path as shown in Fig. 4(b), what we actually measured are the components v_x and D_x projected onto the x-direction in the lab frame. To recover the values useful for the 1D potential discussed in Sec. II, we use the notions $v = v_x/\cos(\pi/6)$ and $D = D_x/\cos^2(\pi/6)$ in the following discussion. Similarly, the force projected along the 1D potential can be written as $F = F_x\cos(\pi/6)$, where F_x is given in Eq. (38). For sample S1, we also measure the drift velocity v_y and diffusion coefficient D_y in the y-direction. It is found that $v_y = 0$, indicating that the detailed balance is still maintained in the transverse transition, in which no external force is applied.

C. Measured mean drift velocity v

We first discuss the measured drift velocity v_0 for the top layer particles used in samples S1 and S2 over a flat incline without any energy barrier ($U_0(X) = 0$) at various tilting angles θ. Figure 6(a) shows the measured v_0 as a function of F for samples S1 (red triangles) and S2 (black squares). In the plot, the measured v_0 is normalized by the thermal velocity $v_T = D_0/\lambda$, where D_0 is the measured diffusion coefficient of the same particles over the flat surface at $\theta = 0$. The force F is normalized by the thermal force $F_T = k_BT/\lambda$. It is seen that the measured v_0 increases linearly with the applied force F for both samples. The dashed line shows the expected equation $v_0/v_T = F/F_T$ (i.e., $v_0 = F/\xi$), which agrees well with the measurements. In the above plot, we used one of the data points to calibrate the buoyancy force Δmg. In this way, all the parameters used in Fig. 6 are the directly measured quantities and hence one can reduce the uncertainties of the nominal value of Δmg provided by the manufacturer.

The blue circles in Fig. 6(a) are the measured v/v_T for sample S2. The error bars indicate the standard deviation of the measurements at each tilt angle. Compared to the black squares, the measured v/v_T for sample S2 is found to be significantly hindered by the underlying potential $U_0(X)$; the measured values of v/v_T are much smaller than the corresponding values of v_0/v_T for a flat incline. The measured v/v_T is first flattened out when the force F is in the range $1 \lesssim F/F_T \lesssim 12$ followed by a curving-up rise in the force range $12 \lesssim F/F_T \lesssim F_c/F_T \simeq 22.8$. When F exceeds its critical value F_c, the measured v begins to approach the asymptotic value v_0 and becomes very close to the measured v_0 when $F/F_T \simeq 60$.

Figure 6(b) shows a comparison of the measured v/v_T between samples S1 and S2. Because F scales with d^3 [see Eq. (38)], the magnitude of F for S1 is only about 1/5 of the value for S2 at the same tilt angle θ. The error bars indicate the standard deviation of the measurements at each tilt angle. While the measured v/v_T for sample S1 is still reduced by the underlying potential, the difference between the measured v and v_0 is small. This is because the barrier height for S1 is comparable to k_BT ($E_b = 1.5k_BT$), so that the critical force F_c is small ($F_c/F_T \simeq 5.9\pm2$ for S1) and so is the hindering effect of the external potential. With the measured potential $U_0(X)$ as shown in Fig. 3, we numerically calculate v as a function of F using Eq. (4). The calculated v for samples S1 and S2 are, respectively, plotted as the green and blue solid lines in Fig. 6. The exact theoretical results agree well with the experimental data for both colloidal samples.

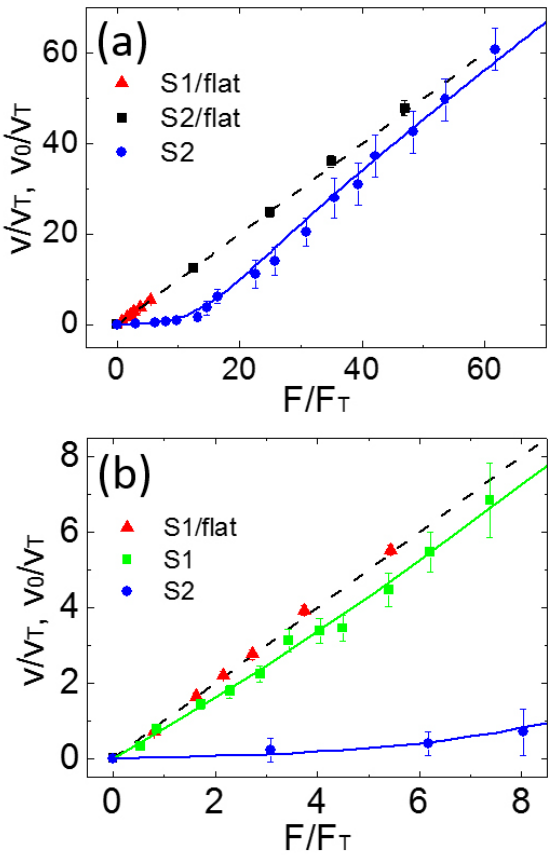

FIG. 6. (color online) (a) Measured drift velocity v_0/v_T and v/v_T as a function of F/F_T for three different samples: (i) $d = 2.14\ \mu m$ silica spheres on a flat incline (S1/flat, red triangles), (ii) $d = 3.6\ \mu m$ silica spheres on a flat incline (S2/flat, black squares with an error bar), and (iii) sample S2 (blue circles with an error bar). The black dashed line is a plot of the equation $v/v_T = F/F_T$. The blue solid line is a numerical plot of Eq. (4) using the measured $U_0(X)$ for S2. (b) An enlarged plot of the measured v_0/v_T and v/v_T as a function of F/F_T for three different samples: (i) $d = 2.14\ \mu m$ silica spheres on a flat incline (S1/flat, red triangles), (ii) sample S1 (green squares with an error bar), and (iii) sample S2 (blue circles with an error bar). The black dashed line is a plot of the equation $v/v_T = F/F_T$. The green and blue solid lines are, respectively, the numerical plots of Eq. (4) using the measured $U_0(X)$ for S1 and S2.

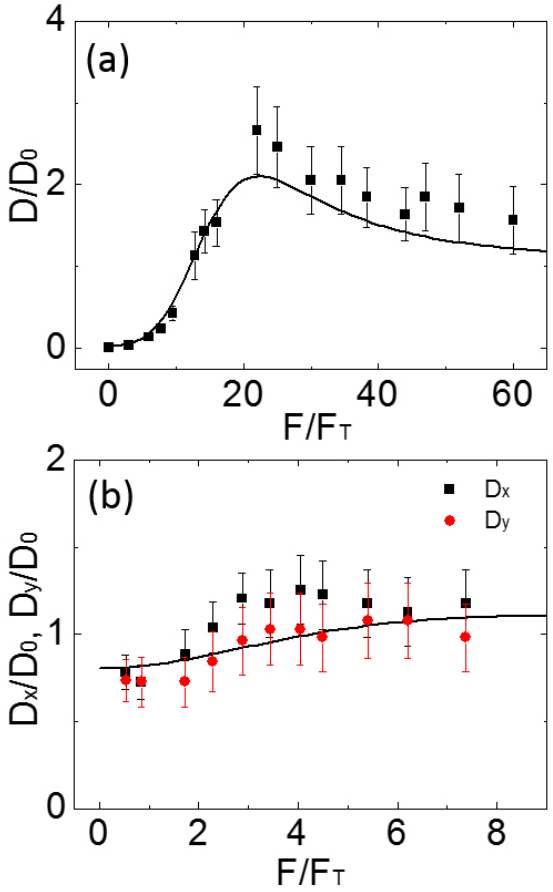

FIG. 7. (color online) (a) Measured diffusion coefficient D/D_0 as a function of F/F_T for sample S2. The error bars indicate the standard deviation of the measurements at each tilt angle. The solid line shows the numerically calculated D/D_0 using Eq. (6) with the measured $U_0(X)$ for S2, as shown in Fig. 3. (b) Measured D_x/D_0 (black squares) and D_y/D_0 (red circles) as a function F/F_T for sample S1. The solid line shows the numerically calculated D/D_0 using Eq. (6) with the measured $U_0(X)$ for S1, as shown in Fig. 3.

D. Measured diffusion coefficient D

Figure 7(a) shows the measured diffusion coefficient D as a function of F for sample S2. In the plot, the measured D [$= D_x/\cos^2(\pi/6)$] along the quasi-1D potential is normalized by $D_0 = 0.065\ \mu m^2/s$, which is the measured diffusion coefficient of the same particles over the flat incline at $\theta = 0$. The force F is normalized by the thermal force F_T. The error bars indicate the standard deviation of the measurements at each tilt angle. The measured D/D_0 at the zero tilt angle ($F = 0$) is $D/D_0 \simeq 0.02 \pm 0.007$, which is in good agreement with the obtained value of $1/R = 0.025 \pm 0.003$ for S2 [see Eq. (9)], as shown in Table I. As F increases, the value of D increases quickly and reaches a peak value of $D_{max}/D_0 \simeq 2.6$ at $F/F_T \simeq 22$, which is very close to the critical force $F_c/F_T = 22.8 \pm 2$ as measured from the potential for sample S2. When F exceeds F_c, the measured D starts to decrease with increasing F. For the largest value of F achieved in experiment ($F/F_T \simeq 60$), we find $D/D_0 \simeq 1.5$. The solid line in Fig. 7(a) shows the numerically calculated D/D_0 using Eq. (6) with the measured $U_0(X)$ for S2, as shown in Fig. 3. The calculated D/D_0 shows a peak at the position $F/F_T \simeq 22$ and is in good agreement with the measured D/D_0 (within the experimental uncertainties). The asymptotic value of D/D_0 should be unity when $F >> F_c$, and we have found that the calculated $D/D_0 \simeq 1.05$ at $F/F_T \simeq 120$ [not shown in Fig. 7(a)].

Figure 7(b) shows the measured diffusion coefficients D_x/D_0 (black squares) and D_y/D_0 (red circles) for sample S1. The error bars indicate the standard deviation of the measurements at each tilt angle. When $F = 0$, we find $D_x/D_0 \simeq D_y/D_0 \simeq 0.75\ \pm 0.2$, which is close to the measured value of $3/(4R) \simeq 0.58$ for S1, as shown in Table I. The numerical prefactor 3/4 is introduced here owing to the fact that for each potential well there are three exits [16]. Because there is no preferred direction in the untilted sample, the diffusion coefficients along the two orthogonal directions are indistinguishable. When the external force F is turned on, the measured D_x/D_0 and D_y/D_0 both increase slowly with F and reach a maximum value when F/F_T is in the range of 4-5. The obtained peak position is close to the calculated critical force $F_c/F_T \simeq 5.9 \pm 2$ using the measured $U_0(X)$ for S1. The obtained maximum value of D_x/D_0 is about 1.2 and that for D_y/D_0 is 1.1. The solid line in Fig. 7(b) shows the numerically calculated D/D_0 using Eq. (6) with the measured $U_0(X)$ for S1, as shown in Fig. 3. The calculated D/D_0 shows a good agreement with the measured D_y/D_0, but the measured D_x/D_0 is notably larger than the 1D theoretical calculation. Figure 7(b) clearly reveals that the enhancement of diffusion in the x-direction is larger than that in the y direction. Our analysis, however, is only semi-quantitative as the particle's trajectories for S1 are not exactly 1D.

E. Scaling behavior of the measured v and D

1. *Steepest descent approximation for small forces*

We now discuss the scaling behavior of the measured drift velocity v and diffusion coefficient D under the steepest descent approximation. When the applied force F is small (i.e., $F/F_T < 1$) and the energy barrier height E_b is large (i.e., $E_b/k_BT >> 1$), both v and D have a similar scaling form, as shown in Eqs. (14) and (15). The dimensional scaling factors are, respectively, $v_0 = F/\xi$ and $D_0 = k_BT/\xi$, which are independent of the potential $U_0(X)$. The common scaling factor $\nu \exp[-E_b/k_BT]$ is of the Arrhenius-Kramers form, which only involves the potential $U_0(X)$ and is independent of the external force F. The scaling form for v and D thus suggests that

in the small F limit, the particle's diffusion remains the same as that at equilibrium ($F = 0$), except that there is a net particle flux, $J_s \propto nv$, along the direction of the external force F, where n is the area fraction occupied by the top layer particles.

2. *Steepest descent approximation for intermediate forces $F_T \lesssim F \lesssim F_c$*

Equations (30) and (35) are the new scaling forms obtained for v and D when the external force is in the intermediate range $F_T \lesssim F \lesssim F_c$. The dimensional scaling factor for v is $v_c = F_c/\xi$, which is the drift velocity of the particle over a flat incline under the influence of the constant force F_c. The dimensional scaling factor for D is $D_c = F_c\lambda/2\xi = v_c\lambda/2$, which is an enhanced diffusion coefficient due to the drift velocity v_c. Compared to the particle's free diffusion coefficient $D_0 = k_BT/\xi$, we find the enhancement factor $D_c/D_0 = F_c/(2F_T)$, which is independent of the thermal energy k_BT. The enhancement factor can also be expressed as the Peclet number $Pe = v_c\lambda/2D_0$, which measures how far the system is driven away from equilibrium by the external force F_c. The value of D_c sets up an upper bound for the peak value of D obtained at $F \simeq F_c$. For example, we find the calculated $D_c/D_0 \simeq 3.1$ for sample S2. The measured peak value of D is $D/D_0 \simeq 2.6$ and the calculated peak value of D at $F \simeq F_c$ using the exact solution in Eq. (6) is $D/D_0 \simeq 2.1$.

The normalized drift velocity v/v_c and diffusion coefficient D/D_c share the common scaling form, $\nu' \exp[-E_b^*/k_BT]$, which is of the Arrhenius-Kramers form, but both the pre-factor ν' and the energy barrier height E_b^* are modified by the external force F. As shown in Eq. (31), the pre-factor ν' only involves F/F_c. This new form of the Arrhenius-Kramers equation has been obtained previously [33] and here we gave an exact proof. Owing to the change of the effective potential to $U(x) = U_0(x) - Fx$, the position of the saddle points is altered and so does the new effective barrier height E_b^*. To calculate E_b^*, one needs to know the functional form of $U_0(x)$. Equation (29) shows an example for the trial function $U_0(x) = (E_b/2)\cos(2\pi x/\lambda)$. In many practical situations of interest, however, one does not know the functional form of $U_0(x)$ a priori. Having a general expression of E_b^* (and ν') for a model potential is, therefore, very useful for the experiment to extract reliable characteristic information about the external potential.

A simple linear-cubic potential of the form [37, 50]

$$U(x) \simeq F_c x - \alpha(x - x_c)^3, \tag{41}$$

where α is a constant proportional to $U_0'''(x_c)$, is often used to approximate the tilted potential $U(x) = U_0(x) - Fx$ near the inflection point x_c [33, 51]. Figure 8 shows a sketch of the linear-cubic potential $U(x)$ for three different characteristic forces F_T (top black curve) $< F_2$ (middle green curve) $< F_c$ (bottom red curve). As

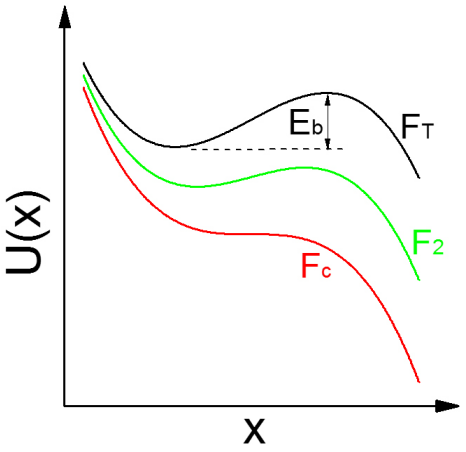

FIG. 8. Sketch of the linear-cubic potential $U(x)$ for three different characteristic forces F_T (top black curve) $< F_2$ (middle green curve) $< F_c$ (bottom red curve). The three curves are displaced vertically for clarity. The intrinsic barrier height E_b is shown for $F = F_T$.

the force F increases, the effective barrier height E_b^* decreases and vanishes at $F = F_c$. Substituting Eq. (41) into Eqs. (23-26), one finds [37]

$$E_b^* = E_b\left(1 - \frac{F}{F_c}\right)^{3/2}, \tag{42}$$

and

$$\nu' = \sqrt{2}\left(1 - \frac{F}{F_c}\right)^{1/2}. \tag{43}$$

Clearly, the expression of E_b^* in Eq. (42) is simpler than that in Eq. (29).

In another simplified model, one assumes that the barrier shape $U_0(x)$ does not change much with Fx under the so-called "sharp barrier" approximation [30, 32]. The main effect of the force F is to change the barrier height from the intrinsic value E_b to

$$E_b^* = E_b - F\frac{\lambda}{2} \simeq E_b\left(1 - \frac{F}{F_c}\right), \tag{44}$$

where $\lambda/2$ is a characteristic distance between the energy minimum and maximum, and $F_c \simeq E_b/(\lambda/2)$ is the critical force. Note that for the tilted cosine potential we find $F_c = \pi E_b/\lambda$, and for the linear-cubic potential one has $F_c = 3E_b/\lambda$. In this simple model, the prefactor ν' was assumed to be a constant equal to the prefactor ν without the influence of the applied force. This model was first proposed by Bell [30] and further improvements were considered recently to include the effect of the force on ν' [33] and corrections in the vicinity of F_c [52].

Figure 9 shows a comparison of the calculated E_b^* as a function of F/F_c using Eq. (29) for the tilted cosine potential (red solid line), Eq. (42) for the linear-cubic potential (black dashed line), and Eq. (44) for the "sharp

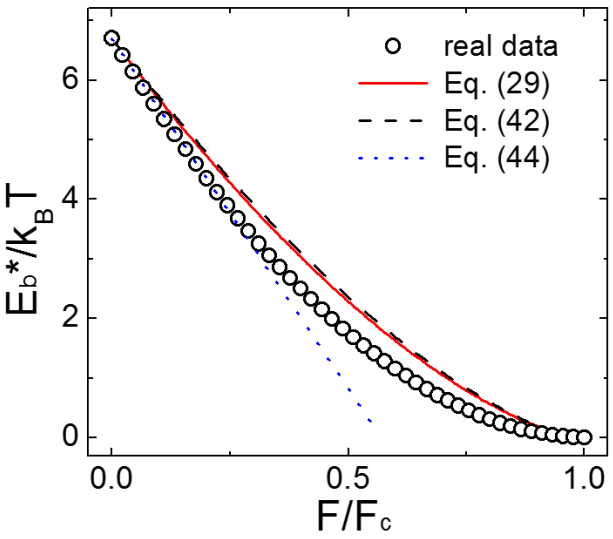

FIG. 9. (color online) Comparison of the calculated barrier height E_b^*/k_BT as a function of F/F_c using Eq. (29) (red solid line), Eq. (42) (black dashed line), and Eq. (44) (blue dotted line) all with $E_b = 6.7k_BT$. The open circles are the obtained values of E_b^*/k_BT using the measured $U(X)$ for sample S2.

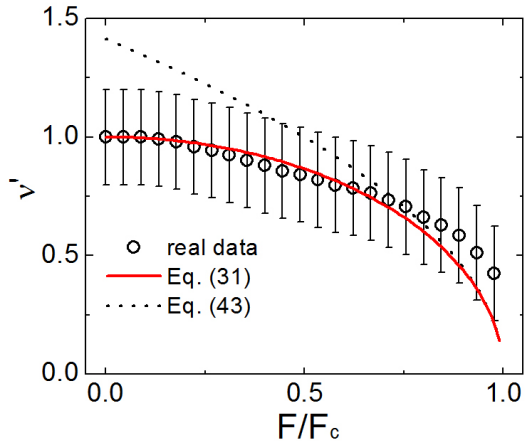

FIG. 10. (color online) Comparison of the calculated prefactor v' as a function of F/F_c using Eq. (31) (red solid line) and Eq. (43) (black dashed line). The open circles are the obtained values of v' using the measured $U(X)$ for sample S2.

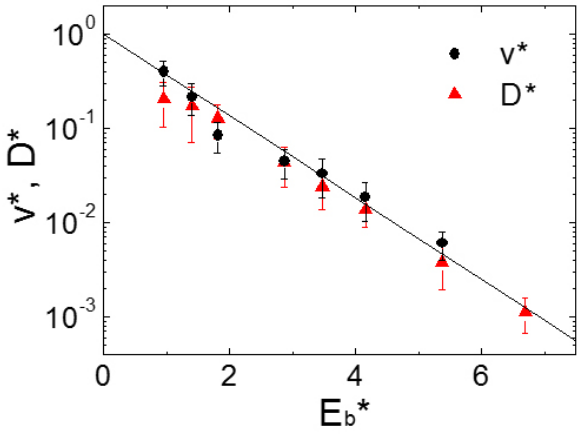

FIG. 11. (color online) Normalized drift velocity $v^* = v/(v_c\nu')$ (black circles) and diffusion coefficient $D^* = D/(D_c\nu')$ (red triangles) as a function of the effective barrier height Eb^*/k_BT for sample S2. The solid line is a plot of the scaling function, $v^*, D^* = \exp[-E_b^*/k_BT]$.

barrier" case (blue dotted line) all with $E_b = 6.7k_BT$. The open circles are the obtained values of E_b^*/k_BT using the measured $U_0(X)$ for sample S2. It is seen that the two curves for the tilted cosine potential and linear-cubic potential are very close to each other and they show little difference in the whole range of $0 \lesssim F/F_c \lesssim 1$. These two curves fit the data at both the small and large force ends but in the middle force range ($F/F_c \simeq 0.5$), the calculated E_b^* is off by $\sim 0.8k_BT$ compared with the measured value. The Bell's expression for the "sharp barrier" case is clearly a good approximation in the small force range. For larger values of F/F_c, Eq. (44) underestimates the true value of E_b^* significantly. Figure 9 thus demonstrates that Eq. (42) gives an upper bound of the measured E_b^*/k_BT, whereas Eq. (44) gives a lower bound of the measured E_b^*/k_BT. Overall, Eq. (42) gives a reasonably good estimate of the effective barrier height E_b^*/k_BT without knowing the fine details of the potential, so long as the critical force F_c is known.

Figure 10 shows a comparison of the calculated ν' as a function of F/F_c using Eq. (31) for the tilted cosine potential (red solid line) and Eq. (43) for the linear-cubic potential (black dashed line). The open circles are the numerically calculated values of $\nu' = (|U_a''U_b''|)^{1/2}\lambda^2/(2\pi k_BT)$, where U_a'' and U_b'' are, respectively, the second derivatives of the tilted potential $U(x) = U_0(x) - Fx$ at the energy minimum x_a and at the energy barrier x_b. The measured values of $U_0(X)$ for sample S2 are used in the numerical calculation. The error bars result mainly from the uncertainties involved in the numerical calculation of U_a'' and U_b''. It is seen that the two calculated curves agree with each other only in the large force end ($F \simeq F_c$), whereas at smaller values of F/F_c the black dashed line for the linear-cubic potential shows a large deviation from the data. The red solid line for the tilted cosine potential fits the data well, except in the vicinity of F_c in which a small deviation is observed. Figure 10 thus demonstrates that Eq. (31) gives a good estimate of the prefactor ν', which is not very sensitive to the fine details of the potential so long as the critical force is known.

With this understanding of the effective barrier height E_b^* and prefactor ν', we now can examine the scaling behavior of the measured drift velocity v and diffusion coefficient D. Figure 11 is a re-plot of the measured $v^* = v/(v_c\nu')$ (black circles) and $D^* = D/(D_c\nu')$ (red

triangles) for sample S2 as a function of E_b^*. In the plot, the measured v and D are normalized, respectively, by $v_c\nu'$ and $D_c\nu'$, where $v_c = F_c/\xi$, $D_c = F_c\lambda/\xi$ and $\nu' = [1-(F/F_c)^2]^{1/2}$ are all calculated using the value of F_c obtained at the peak position of the measured D, as shown in Fig. 7(a). The values of E_b^* are obtained using Eq. (42) with the measured values of E_b and F_c for S2 given in Table I. It is seen that the two sets of data overlap with each other well, indicating that they share the same scaling form. The solid line is a plot of the scaling function $v^*, D^* = \exp[-E_b^*/k_BT]$, which fits data well, especially in the region with $E_b^*/k_BT \gtrsim 3$. It has been shown recently [16] that the inclusion of the (modified) Arrhenius factor ν' in the scaling plot helps to reduce deviations of the data from the simple exponential function for small values of E_b^*/k_BT. Figure 11 thus verifies the scaling behavior of the measured v and D, as predicted in Eqs. (30) and (35).

3. *Approximations in the $F > F_c$ regime*

While the scaling behavior of the measured v and D improves in general for larger values of F when F is in the intermediate range $F_T \lesssim F \lesssim F_c$, the steepest descent approximation will eventually become invalid when F is getting so close to F_c that the effective barrier height becomes very small ($E_b^*/k_BT \lesssim 1$). Figures 12(a) and 12(b) show, respectively, comparisons between the calculated scaling functions and the exact solution of v/v_c and D/D_c as a function of F/F_c for the tilted cosine potential with $E_b = 6.7k_BT$. The calculations are made under three different approximations. The black solid lines in Figs. 12(a) and 12(b) show, respectively, the numerical results of the exact solutions of v/v_c in Eq. (4) and D/D_c in Eq. (6), for the tilted cosine potential with $E_b = 6.7k_BT$. The green dash-dotted lines show the same scaling solution in Eq. (30) [or in Eq. (35)] with E_b^* and ν' being given, respectively, in Eqs. (42) and (43) for the linear-cubic potential. The red dashed line in Fig. 12(a) shows the scaling solution in Eq. (30) with E_b^* and ν' being given, respectively, in Eqs. (29) and (31) for the tilted cosine potential.

It is seen from Fig. 12(a) that while the red dashed line follows the exact solution slightly better than the green dash dotted line (as its E_b^* and ν' are calculated particularly for the tilted cosine potential), the two scaling solutions are very close with each other over the entire force range $0 \le F/F_c \le 1$. Both the scaling solutions, however, show significant deviations from the exact solution of v/v_c (and D/D_c) when F approaches to F_c, at which $E_b^* = 0$ and $\nu' = 0$. Figures 12(a) and 12(b) reveal that the scaling solution in Eq. (30) follows the exact solution of v/v_c over a larger range of F/F_c up to $F/F_c \lesssim 0.9$, whereas it can only follow the exact solution of D/D_c up to $F/F_c \lesssim 0.5$. From the exact solutions of v/v_c and D/D_c, one finds that they have different asymptotic behavior when $F/F_c > 1$.

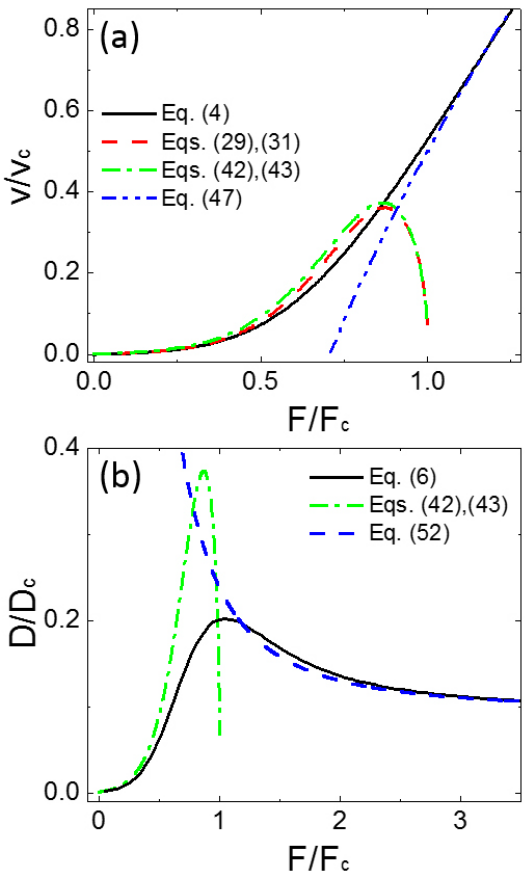

FIG. 12. (color online) (a) Comparison between the calculated scaling functions and the exact solution of v/v_c as a function of F/F_c for the tilted cosine potential with $E_b = 6.7k_BT$. The calculations are made under different approximations: (i) exact solution of v/v_c in Eq. (4) (black solid line), (ii) scaling solution in Eq. (30) with E_b^* and ν' being given, respectively, in Eqs. (29) and (31) for the tilted cosine potential (red dashed line), and (iii) scaling solution in Eq. (30) with E_b^* and ν' being given, respectively, in Eqs. (42) and (43) for the linear-cubic potential (green dash-dotted line). The blue dot-dot dashed line shows the approximate expression in Eq. (47) for $F > F_c$. (b) Comparison between the calculated scaling functions and the exact solution of D/D_c as a function of F/F_c for the tilted cosine potential with $E_b = 6.7k_BT$. The calculations are made under different approximations: (i) exact solution of D/D_c in Eq. (6) (black solid line), and (ii) scaling solution in Eq. (35) with E_b^* and ν' being given, respectively, in Eqs. (42) and (43) for the linear-cubic potential (green dash-dotted line). The blue dashed line shows the approximate expression in Eq. (52) for $F > F_c$.

We now derive an approximate expression for $v(F, E_b)$ in the $F > F_c$ regime. As mentioned above, the critical force F_c is given by the positive root of $F_c = U_o'(x_c)$, where x_c is the point of inflexion of U given by $U_o''(x_c) = 0$. For $U_o(x) = \frac{E_b}{2}u(x)$, we have $F_c = \frac{E_b}{2}u'(x_c)$. When $F > F_c$, $g_1(x, y)$ in Eq. (18) has no saddle point or local extremum in the λ^2 square. The minimal value of $g_1(x, y)$

on the $\lambda \times \lambda$ square is at $y = 0$ with $g_1(x, 0) = 0$. Hence the integral $\int_0^\lambda dy \exp[-\frac{E_b}{2k_BT} g_1(x, y)]$ is dominated by the $y \gtrsim 0$ region, and one can expand near $y = 0$ to get $g_1(x, y) \simeq [2F/E_b - u'(x)]y + \mathcal{O}(y^2)$. Therefore, one has

$$\frac{1}{\lambda}\int_0^\lambda dy e^{-\frac{E_b g_1(x,y)}{2k_BT}} \simeq \frac{1 - e^{[-F\lambda + E_b u'(x)/2]/k_BT}}{[F\lambda - E_b u'(x)/2]/k_BT}. \quad (45)$$

For $F > F_c = \frac{E_b}{2} u'(x_c)$ and keeping the leading orders in F, one obtains an approximate expression for the scaled velocity,

$$\frac{v}{v_c} \simeq \frac{F}{F_c} - \frac{\overline{u'^2}}{[u'(x_c)]^2}\frac{F_c}{F} + \mathcal{O}\left[\left(\frac{F_c}{F}\right)^2\right], \quad (46)$$

where $\overline{u'^2} \equiv \frac{1}{\lambda}\int_0^\lambda [u'(x)]^2 dx$.

For $u(x) = \cos(2\pi x/\lambda)$, one has

$$\frac{v}{v_c} \simeq \frac{F}{F_c} - \frac{F_c}{2F}. \quad (47)$$

Equation (47) is plotted in Fig. 12(a) (blue dot-dot dashed line) to compare with the exact result. It is seen that the approximate expression in Eq. (47) holds very well up to $F \gtrsim F_c$. Note that the above result can be interpreted in terms of the effective friction coefficient

$$\xi_{eff}(F) \simeq \xi[1 + \left(\frac{E_b}{2F}\right)^2 \overline{u'^2} + \cdots], \quad (48)$$

for $F > F_c$.

Similarly, when $F > F_c$, $g_2(x, y, w, z)$ in Eq. (20) also has no saddle point or local extremum in the λ^4 hypercube and its minimal value is $g_2(x, 0, 0, 0)$. Thus one can expand $g_2(x, y, w, z)$ around $y = z = w = 0$ to get

$$g_2(x, y, w, z) \simeq \left[\frac{2F}{E_b} - u'(x)\right](y + w + z) + \cdots. \quad (49)$$

Hence

$$\begin{aligned}
&\frac{1}{\lambda}\int_0^\lambda dx I_+^2(x) I_-(x) \\
&\simeq \frac{1}{\lambda}\int_0^\lambda dx \left[\frac{1}{\lambda}\int_0^\lambda dy e^{[-F + \frac{E_b}{2}u'(x)]y/(k_BT)}\right]^3 \\
&\simeq \left(\frac{k_BT}{F\lambda}\right)^3 \left[1 + 6\left(\frac{E_b}{2F}\right)^2 \overline{u'^2} + \cdots\right]. \quad (50)
\end{aligned}$$

Using Eq. (6), one finally obtains

$$\frac{D}{D_c} \simeq \frac{2k_BT}{F_c\lambda}\left[1 + 3\left(\frac{F_c}{F}\right)^2 \frac{\overline{u'^2}}{[u'(x_c)]^2}\right]. \quad (51)$$

For $u(x) = \cos(2\pi x/\lambda)$, we find

$$\frac{D}{D_c} \simeq \frac{2k_BT}{F_c\lambda}\left[1 + \frac{3}{2}\left(\frac{F_c}{F}\right)^2\right]. \quad (52)$$

Equation (52) is plotted in Fig. 12(b) (blue dashed line) to compare with the exact result. It is seen that the approximate expression in Eq. (52) holds well for $F > F_c$.

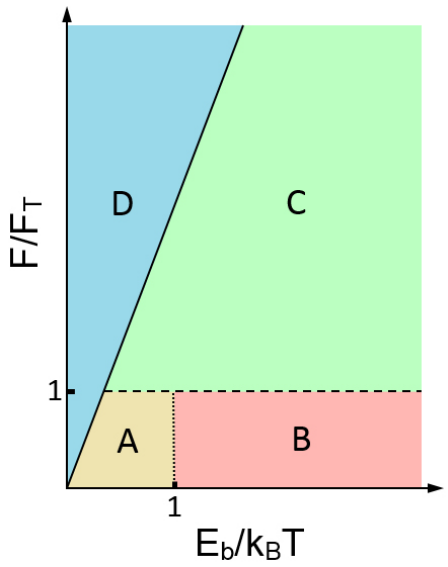

FIG. 13. (color online) Overall "phase diagram" of the colloidal transport and diffusion dynamics over a tilted periodic potential in the plane of the normalized external force F/F_T and intrinsic barrier height E_b/k_BT. The black solid line indicates $F/F_T = \pi E_b/k_BT$ (i.e., $F = F_c$). The black dashed line indicates $F/F_T = 1$ and the black dotted line indicates $E_b/k_BT = 1$. The entire phase diagram is divided by the three lines into four (colored) regions, A (yellow), B (pink), C (light green), and D (light blue), each representing a unique dynamic phase (see text for more details).

4. *Scaling regions of the measured v and D*

Based on the above discussion, we now can characterize the dynamics of colloidal diffusion over a tilted periodic potential in a 2D "phase diagram," as shown in Fig. 13. The phase diagram is plotted as a function of the normalized external force F/F_T and intrinsic energy barrier height E_b/k_BT. The black solid line indicates $F/F_T = \pi E_b/k_BT$ (i.e., $F = F_c$). The critical force F_c scales with $E_b/(\lambda/2)$ and here $\pi/2$ is used as an indicative prefactor. The black dashed line indicates $F/F_T = 1$ and the black dotted line indicates $E_b/k_BT = 1$. The entire phase diagram is divided by the three lines into four (colored) regions, A (yellow), B (pink), C (light green), and D (light blue), each representing a unique dynamic phase.

In region A (yellow) where both F/F_T and E_b/k_BT are small, the small force expansion of Eqs. (8) and (9) can be used to describe the dynamics of colloidal diffusion as measured by the mean drift velocity v and diffusion coefficient D. In region B (pink) where F/F_T is small but E_b/k_BT is large, Eqs. (8) and (9) can be further simplified under the steepest descent approximation. As a result, both the normalized drift velocity v/v_0 and diffusion coefficient D/D_0 share the same scaling form of Arrhenius-Kramers type at the lowest order of F/F_T, as shown in Eqs. (14) and (15). Between the solid line

$F = F_c$ and the dashed line $F = F_T$ is region C (light green), in which the tilted potential $U(x)/k_BT$ is large enough so that the steepest descent approximation applies. In this case, the normalized drift velocity v/v_c and diffusion coefficient D/D_c share the same scaling form as shown in Eqs. (30) and (35). While the scaling function is of Arrhenius-Kramers form, both the pre-factor $\nu'(F)$ and the effective barrier height $E_b^*(F)$ are modified by the external force F. It is found that Eq. (42) provides a simple (upper bound) estimate on how $E_b^*(F)$ varies with F/F_c, whereas Eq. (44) only gives a linear expansion of $E_b^*(F)$ for small values of F/F_c. We also find that Eq. (31) provides a good estimate on how ν' varies with F/F_c. In region D (light blue) where $F/F_c \gtrsim 1$, the effect of the external force F is dominant over the potential $U_0(x)$ and the dynamics of colloidal diffusion become similar to that over a flat incline. As discussed above, the boundaries between different dynamic phases are not sharp and care needs to be taken for the crossover between different phases.

V. SUMMARY

We have constructed a two-layer colloidal system for the study of diffusive and force-assisted barrier-crossing dynamics over a periodic potential. The micron-sized particles on the bottom layer form a colloid crystal, whose corrugated surface provides a gravitational potential field for the top layer diffusing particles. When the colloidal sample is carefully leveled, the top layer particles are under no external force and their motion over the periodic potential is made under constant thermal agitations. Using the techniques of optical microscopy and multi-particle tracking, we measured the population probability histogram $P(x, y)$ of the top layer diffusing particles, from which one finds the underlying potential $U_0(x, y)$ via the Boltzmann distribution, as shown in Eq. (39). By averaging over the repetitive units of the colloidal crystal and simplifying the periodic potential into a quasi-1D barrier function $U_0(X)$, we were able to improve the statistical accuracy of $U_0(X)$ down to $\sim 0.1k_BT$.

When the colloidal sample is tilted at an angle θ (in the range of 0-35°) with respect to the vertical (gravity) direction, a tangential component of the gravitational force F is applied to the diffusing particles. This external force reduces the energy barrier height so that the detailed balance for the diffusing particles is broken and a net particle flux is generated along the direction of forcing. From the measured particle trajectories, we calculated the probability density function $G(\Delta x, \tau)$ of the particle's displacement $\Delta x(\tau)$, from which one obtains the mean drift velocity $v(F, E_b)$ and diffusion coefficient $D(F, E_b)$ of the particles as a function of F and intrinsic barrier height E_b. The measured $v(F, E_b)$ and $D(F, E_b)$ are in good agreement with with the exact results of the 1D drift velocity [1] and diffusion coefficient [2, 3].

Based on these exact results, we analytically showed under the steepest descent approximation that there exists a scaling region, in which $v(F, E_b)$ and $D(F, E_b)$ both scale as $\nu'(F)\exp[-E_b^*(F)/k_BT]$, where the pre-factor $\nu'(F)$ and barrier height $E_b^*(F)$ both are modified by F. The experiment verified the theory and demonstrated the applications of the colloidal potential. With the simultaneously obtained energetics and dynamics information, we examined different scaling forms of $\nu'(F)$ and $E_b^*(F)$ and their accuracy in determining the characteristics of the external potential, such as the intrinsic barrier height E_b.

It was found that in the small F region, the effect of the potential $U_0(x)$ can be separated from the external force F, and both $v(F, E_b)$ and $D(F, E_b)$ can be expanded in terms of F/F_T. In the intermediate force region ($F_T < F < F_c$), the normalized $v(F, E_b)$ and $D(F, E_b)$ share the same scaling form of Arrhenius-Kramers type, as discussed above. The effective barrier height $E_b^*(F)$ is lowered by the external force F. In the large force limit ($F/F_c \gtrsim 1$), the effect of the potential $U_0(x)$ becomes very small and the dynamics of colloidal diffusion is similar to that over a flat incline. Furthermore, a "phase diagram" of the colloidal transport and diffusion dynamics over a tilted periodic potential is drawn in the plane of the normalized external force F/F_T and intrinsic barrier height E_b/k_BT. The phase diagram provides a useful guideline about the dynamic behavior and effective governing equations for the colloidal transport and diffusion in the linear and nonlinear regimes of the applied force.

This work provided crucial information for our general understanding of forced barrier-crossing dynamics beyond the linear response theory and the Arrhenius-Kramers equation. In addition, our results provided a useful interpretation of the driven colloidal transport in terms of a force-dependent effective friction coefficient $\xi_{eff}(F)$ given by Eqs. (16), (32) and (48), respectively, as the forcing increases. By carefully examining the theoretical and experimental results, we find that the Stokes-Einstein relation between the diffusion coefficient D and the friction coefficient ξ_{eff} in the steady-state is violated to a different extend, depending on the driving or how far away from equilibrium. In the small F region, the particles spend most of their time near the local minima of the tilted periodic potential with occasional hopping to the next well. The system is still very much thermalized and close to equilibrium and thus the Stokes-Einstein relation holds. In the intermediate force region, the external driving is strong enough to cause rapid hopping and thus the particles do not have much time to be thermalized in the local minima. In this case, D still has the Stokes-Einstein form, but the energy input $F\lambda/2$ becomes the dominant source causing diffusion and friction. In the large force limit, the system is far from equilibrium and k_BT plays no role at all. In this case, D and ξ_{eff} are not related by any Stokes-Einstein-like relation, except in the $F \to \infty$ limit in which the usual Stokes-Einstein relation recovers: $D \to D_0$.

ACKNOWLEDGMENTS

PYL thanks the support by Ministry of Science and Technology of Taiwan under Grant no. 101-2112-M-008-004-MY3 and NCTS of Taiwan. PT was supported by the Hong Kong Research Grants Council under Grant no. HKUST-16305214. PT and PYL also acknowledge the support in part by the Kavli Institute for Theoretical Physics China during their stay.

[1] R. L. Stratonovich, Radiotekh. Elektron. **3**, 497 (1958).
[2] P. Reimann, C. Van den Broeck, H. Linke, P. Hanggi, M. Rubi and A. Perez-Madrid, Phys. Rev. Lett. **87**, 010602 (2001).
[3] P. Reimann, C. Van den Broeck, H. Linke, P. Hanggi, M. Rubi and A. Perez-Madrid, Phys. Rev. E **65**, 031104 (2002).
[4] P. Hanggi, P. Talkner and M. Borkovec, Rev. Mod. Phys. **62**, 251 (1990).
[5] G. Ayrault and G. Ehrlich, J. Chem. Phys. **60**, 281 (1973).
[6] Z. Y. Zhang and M. G. Lagally, Science, **276**, 377 (1997).
[7] J. Repp, G. Meyer, F. E. Olsson and M. Persson, Science, **305**, 493 (2004).
[8] F. Zhang, G. M. Lee and K. Jacobson, BioEssays **15**, 579 (1993).
[9] K. Jacobson, E. D. Sheets and R. Simson, Science **268**, 1441 (1995).
[10] R. L. Baldwin, Nature, **369**, 183 (1994).
[11] R. L. Baldwin, J. Biomol NMR, **5**, 103 (1995).
[12] S. Arrhenius, Z. Phys. Chem. **4**, 226(1889).
[13] H. A. Krammers, Physica **7**, 284(1940).
[14] J. V. Barth, H. Brune, B. Fischer, J. Weckesser and K. Kern, Phys. Rev. Lett. **84**, 1732 (2000).
[15] G. L. Hunter and E. R. Weeks, Phys. Rev. E **85**, 031504 (2012).
[16] X.-G. Ma, P.-Y. Lai and P. Tong, Soft Matter **9**, 8826 (2013).
[17] A. Ajdari and J. Prost, Proc. Natl. Acad. Sci. USA. **88**, 4468 (1991).
[18] G. I. Nixon and G.W. Slater, Phys. Rev. E 53, 4969 (1996).
[19] D. C. Yeh and H. B. Huntington, Phys. Rev. Lett. **53**, 1469 (1984).
[20] A. V. Latyshev, A. L. Aseev, A. B. Krasilnikov and S. I. Stenin, Surf. Sci. **213**, 157 (1989).
[21] D. Duvivier, T. D. Blake and J. De Coninck, Langmuir, **29**, 10132 (2013).
[22] O. Pierre-Louis and M. I. Haftel, Phys. Rev. Lett. **87**, 048701 (2001).
[23] K. Svensson, H. Olin, and E. Olsson, Phys. Rev. Lett. **93**, 145901 (2004).
[24] S. Coh, W. Gannett, A. Zettl, M. L. Cohen, and S. G. Louie, Phys. Rev. Lett. **110**, 185901 (2013).
[25] S. B. Smith, Y. J. Cui and C. Bustamante, Science **271**, 795 (1996).
[26] J. Liphardt, B. Onoa, S. B. Smith, I. Tinoco Jr., C. Bustamante, Science **292**, 733 (2001).
[27] M. T. Woodside, P. C. Anthony, W. M. Behnke-Parks, K. Larizadeh, D. Herschlag and S. M. Block, Science **314**, 1001 (2006).
[28] R. Merkel, P. Nassoy, A. Leung, K. Ritchie and E. Evans, Nature **397**, 50 (1999).
[29] R. Berkovich,S. Garcia-Manes, M. Urbakh, J. Klafter and J. M. Fernandez, Biophysical J. **98**, 2692 (2010).
[30] G. I. Bell, Science **200**, 618 (1978).
[31] U. S. Schwarz and S. A. Safran, Rev. Mod. Phys. **85**, 1327 (2013).
[32] Evan Evans, Annu. Rev. Biophys. Biomol. Struct. **30**, 105 (2001).
[33] H. J. Lin, H. Y. Chen, Y. J. Sheng, and H. K. Tsao, Phys. Rev. Lett. **98**, 088304 (2007).
[34] H. Y. Chen and Y. P. Chu, Phys. Rev. E **71**, 010901 (2005).
[35] O. K. Dudko, A. E. Filippov, J. Klafter and M. Urbakh, Proc. Natl. Acad. Sci. USA **100**, 11378 (2003).
[36] Z. Tshiprut and M. Urbakh, J. Chem. Phys. **130**, 084703 (2009).
[37] A. Garg, Phys. Rev. B **51**, 15592 (1995).
[38] R. Nevo, V. Brumfeld, R. Kapon, P. Hinterdorfer and Z. Reich, EMBO reports, **6**, 482 (2005).
[39] H. Frauenfelder, S. G. Sligar and P. G. Wolynes, Science, **254**, 1598 (1991).
[40] P. G. Wolynes, J. N. Onuchic and D. Thirumalai, Science, **267**, 1619 (1995).
[41] D. J. Wales, M. A. Miller and T. R. Walsh, Nature, **394**, 758 (1998).
[42] V. Blickle, T. Speck, U. Seifert, and C. Bechinger, Phys. Rev. E **75**, 060101 (2007).
[43] M. Siler and P. Zemanek, New J. Phys. **12**, 083001 (2010).
[44] R. D. L. Hanes, C. Dalle-Ferrier, M. Schmiedeberg, M. C. Jenkins, and S. U. Egelhaaf, Soft Matter **8**, 2714 (2012).
[45] M. P. N. Juniper, R. Besseling, D. G. A. Aarts, and R. P. A. Dullens, Opt. Exp. **20**, 28707 (2012).
[46] P. Langevin, C. R. Acad. Sci. (Paris) **146**, 530 (1908).
[47] F. Reif, *Fundamentals of Statistical and Thermal Physics* (McGraw-Hill, Auckland, 1985).
[48] S. Lifson and J. L. Jackson, J. Chem. Phys. **36**, 2410 (1962).
[49] J. C. Crocker and D. G. Grier, J. Colloid Interface Sci. **179**, 298 (1996).
[50] J. Kurkijarvi, Phys. Rev. B **6**, 832 (1972).
[51] R. W. Friddle, Phys. Rev. Lett. **100**, 138302 (2008).
[52] O. K. Dudko, G. Hummer, and A. Szabo, Phys. Rev. Lett. **96**, 108101 (2006).